

Experimental observation of partial parity-time symmetry and its phase transition with a laser-driven cesium atomic gas

Yongmei Xue,^{1,*} Chao Hang^{2,3,4,*} Yunhui He,¹ Zhengyang Bai² Yuechun Jiao,^{1,4}
Guoxiang Huang^{2,3,4,†} Jianming Zhao,^{1,4,‡} and Suotang Jia^{1,4}

¹State Key Laboratory of Quantum Optics and Quantum Optics Devices, Institute of Laser Spectroscopy, Shanxi University, Taiyuan 030006, China

²State Key Laboratory of Precision Spectroscopy, East China Normal University, Shanghai 200062, China

³NYU-ECNU Joint Institute of Physics, New York University Shanghai, Shanghai 200062, China

⁴Collaborative Innovation Center of Extreme Optics, Shanxi University, Taiyuan, Shanxi 030006, China



(Received 5 August 2021; accepted 21 April 2022; published 17 May 2022)

Realizing and manipulating parity-time (\mathcal{PT}) symmetry in multidimensional systems are highly desirable for the exploration of nontrivial physics and the discovery of exotic phenomena in non-Hermitian systems. Finding non-Hermitian systems that still have all-real spectra even if their Hamiltonians possess only partial \mathcal{PT} symmetry has also attracted tremendous attention in recent years. Here, we report the experimental observation of partial \mathcal{PT} symmetry in a cesium atomic gas coupled with laser fields, where a two-dimensional partially \mathcal{PT} -symmetric optical potential for a probe laser beam is created. A transition of the partial \mathcal{PT} symmetry from an unbroken phase to a broken one is observed through changing the beam-waist ratio of the control and probe laser beams, and the domains of unbroken, broken, and nonpartial \mathcal{PT} phases are also discriminated unambiguously. Moreover, we develop a technique to precisely determine the exceptional point location of the partial \mathcal{PT} symmetry breaking by measuring the asymmetry degree of the probe-beam intensity distribution. The findings reported here pave the way for controlling multidimensional laser beams in non-Hermitian systems via laser-induced atomic coherence, and have potential applications for designing light amplifiers and attenuators in different parts of laser beams.

DOI: [10.1103/PhysRevA.105.053516](https://doi.org/10.1103/PhysRevA.105.053516)

I. INTRODUCTION

Non-Hermitian Hamiltonians with parity-time (\mathcal{PT}) symmetry can exhibit entirely real spectra [1–3], which provide an excellent platform for uncovering exotic behaviors in open systems and unveiling intriguing prospects of non-Hermitian physics [4–7]. In optics, they have been realized in various physical settings including waveguides and fiber arrays [8–14], photonic circuits and lattices [15,16], microtoroid resonators [17–19], and trapped ions [20]. Among these settings, atomic media are highly desirable for realizing \mathcal{PT} -symmetric Hamiltonians due to their nice coherence property and superiority for active manipulations on selections of atomic levels, light absorption, gain, dispersion, nonlinearity, and so on [21–28].

Note that, to have an all-real spectrum for a non-Hermitian Hamiltonian, the condition of \mathcal{PT} symmetry is neither sufficient nor necessary. When non-Hermiticity increases, the spectrum of a \mathcal{PT} -symmetric Hamiltonian will become complex, indicating a phase transition from an unbroken \mathcal{PT} phase to a broken one. At the transition point in between, the so-called exceptional point (EP), both eigenstates and

eigenvalues coalesce [29,30]. So far, many interesting properties and promising applications have been found for \mathcal{PT} -symmetric systems and EPs therein [31–52]. Moreover, thanks to the fast developments in both theoretical and experimental investigations on Floquet physics and nonequilibrium thermodynamics with ultracold atoms [53–58], the non-Hermitian Floquet systems and related EPs and skin effect have been proposed and have attracted growing attention in the last few years [59,60].

\mathcal{PT} -symmetric Hamiltonians, however, belong only to a small subclass of non-Hermitian Hamiltonians that possess all-real spectra [6]. In recent theoretical works, multidimensional potentials invariant under complex conjugation and reflection in only one direction [e.g., $V^*(x, y) = V(-x, y)$ or $V^*(x, y) = V(x, -y)$ in two dimensions], called *partially* \mathcal{PT} -symmetric potentials, have been found to support all-real spectra [61–63] and display also phase transitions from the unbroken phase to the broken one. The study of partial \mathcal{PT} symmetry can provide a way for realizing multidimensional potentials with all-real spectra without imposing strict \mathcal{PT} -symmetry conditions, and extend greatly the research scope of non-Hermitian systems with all-real spectra beyond one dimension [64].

In this work, we report the experimental observation of partial \mathcal{PT} symmetry. We consider a probe and a control laser beam acting on the cesium atoms in the cell, constituting a three-level Raman scheme. The control beam covers the

*These authors contributed equally to this work.

†Corresponding author: gxhuang@phy.ecnu.edu.cn

‡Corresponding author: zhaojm@sxu.edu.cn

whole probe beam whereas the repumping beam covers only the right-half region of the probe beam, resulting in gain and loss in different parts of the probe beam and hence the creation of a two-dimensional (2D) partially \mathcal{PT} -symmetric potential for the probe beam propagation.

Furthermore, a transition of the partial \mathcal{PT} symmetry from an unbroken phase to a broken one is observed through adjusting the beam-waist ratio of the control and probe beams; the domains of unbroken, broken, and nonpartial \mathcal{PT} phases are demarcated; a technique for precisely determining the EP location of the partial \mathcal{PT} symmetry is developed through the measurement of the asymmetry degree of the probe intensity distribution; and theoretical analysis and numerical simulation based on Maxwell-Bloch equations are carried out which reproduce the experimental observations well. The results on the partial \mathcal{PT} symmetry and its phase transition reported here open a route for actively manipulating multidimensional laser beams in non-Hermitian systems, and have potential applications for designing optical devices with light amplifying and attenuating in different parts of laser beams.

The remainder of the article is arranged as follows. In Sec. II, we describe the experimental setup of the present study and illustrate how to observe the partial \mathcal{PT} symmetry in a cesium atomic vapor cell. In Sec. III, we carry out theoretical analysis and numerical simulations, which are in a good agreement with experimental results. Some related examples of applications are also discussed in this section. Finally, in Sec. IV we summarize the main results obtained in this work.

II. EXPERIMENTAL OBSERVATION OF THE PARTIAL \mathcal{PT} SYMMETRY

A. Experimental setup

The schematic of the experimental setup and the related atomic excitation scheme is shown in Fig. 1. The experiment is performed with a cesium vapor cell of length 2 cm and diameter 2.5 cm. A weak probe and a strong control beam (with half Rabi frequencies Ω_p and Ω_c [65], respectively) are overlapped and copropagate through the cell [see Fig. 1(b)]. They drive the atomic transitions $|1\rangle \rightarrow |3\rangle$ and $|2\rangle \rightarrow |3\rangle$, respectively, with detunings given by $\Delta_3 = \omega_p - (E_3 - E_1)/\hbar$ and $\Delta_2 = \omega_p + \omega_c - (E_2 - E_1)/\hbar$, where E_α is the eigenenergy of the atomic level $|\alpha\rangle$ ($\alpha = 1, 2, 3$) [Fig. 1(a)]. In the experiment, we set $\Delta_2 = 0$ for avoiding the strong dispersion effect while retaining the two-photon absorption, and $\Delta_3/2\pi = 607$ MHz for avoiding the inhomogeneous broadening resulting from the Doppler effect (see Appendix B for more details). The repumping laser is resonant with $|1\rangle \rightarrow |3\rangle$ transition.

Both the probe and the control beams are of Gaussian profiles and their $1/e^2$ waists are w_p and w_c , respectively. The beam-waist ratio of the control and probe beams is $\sigma \equiv w_c/w_p$, which is varied between 1.5 and 5 by tuning the waist of the control beam while keeping $w_p = 110$ μm . The repumping laser (half Rabi frequency Ω_r) has an elliptical Gaussian profile with $1/e^2$ waist $w_{r1} = 200$ μm ($w_{r2} = 700$ μm) for the short (long) axis. It counterpropagates through the cell and covers half of the probe and control beams [see the inset of Fig. 1(b)]. In this way, a 2D

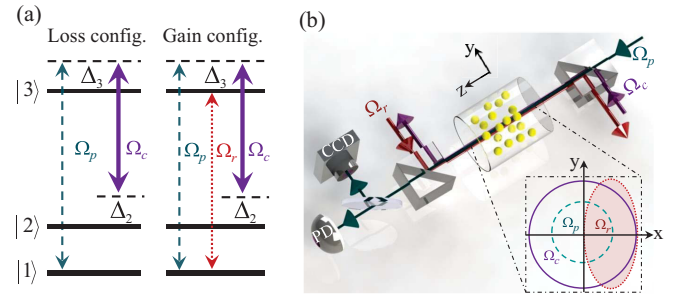


FIG. 1. Experimental design for observing the partial \mathcal{PT} symmetry and its phase transition. (a) Three-level excitation scheme of cesium atoms. The left and right panels show the loss and gain configurations, respectively; Ω_α ($\alpha = p, c, r$) are laser beam Rabi frequencies and Δ_β ($\beta = 2, 3$) are frequency detunings. (b) Sketch of the experimental setup. The control beam covers the whole probe beam whereas the repumping beam covers the right-half region of the probe beam (see the inset), which creates a 2D partially \mathcal{PT} -symmetric potential for the probe beam. The output probe beam is detected with a photodiode and a charge coupled device camera.

optical potential with the partial \mathcal{PT} symmetry [i.e., $V^*(x, y) = V(-x, y)$] for the probe propagation is realized. After passing through the vapor cell, the probe beam is detected by a photodiode (PD) for monitoring its absorption and detected by a charge coupled device (CCD) for attaining its intensity distribution. The atomic density \mathcal{N}_a can be changed by varying the temperature of the cell placed in a thermal chamber (for more details, see Appendix A).

B. Observation of the partial \mathcal{PT} symmetry and its phase transition

In the absence of the repumping beam, the probe beam experiences a loss (i.e., an absorption), which gives a PD signal S_L ; in the presence of the repumping beam it experiences respectively a gain and a loss in the right- and left-half regions, which gives a PD signal S_{GL} . When the gain and loss are exactly balanced, the PD signal S_{GL} would be zero.

Shown in the upper part of Fig. 2(a) is the measured result of the probe intensity distribution from the CCD in the presence of the repumping beam for $\sigma = 2.14$. The intensity distribution is uniform (nonuniform) when $T < 29^\circ\text{C}$ ($T \gtrsim 29^\circ\text{C}$) [66]. The degree of asymmetry of the distribution for $T \gtrsim 29^\circ\text{C}$ increases rapidly as T increases, which becomes the most evident at $T = 45^\circ\text{C}$; i.e., the intensity displays clearly half-dark (left) and half-bright (right) distribution. The orange circles shown in Fig. 2(a1) are results of the probe absorption (i.e., signal S_{GL}) measured from the PD as a function of T (\mathcal{N}_a). We see that S_{GL} keeps nearly zero for $T < 29^\circ\text{C}$ (or $\mathcal{N}_a < 6.29 \times 10^{10} \text{ cm}^{-3}$), indicating that the gain and loss are balanced and hence the system works in a regime of partial \mathcal{PT} symmetry (marked by the shaded region in the figure); S_{GL} begins to increase for $T \gtrsim 29^\circ\text{C}$, indicating that the gain-loss balance is lost and thus nonuniform intensity distribution occurs [corresponding to the lower row of Fig. 2(a)].

Note that the nonuniformity (or asymmetry) of the probe intensity shown in Fig. 2(a) increases smoothly when $T \gtrsim 29^\circ\text{C}$, which is not due to the breaking of the partial \mathcal{PT}

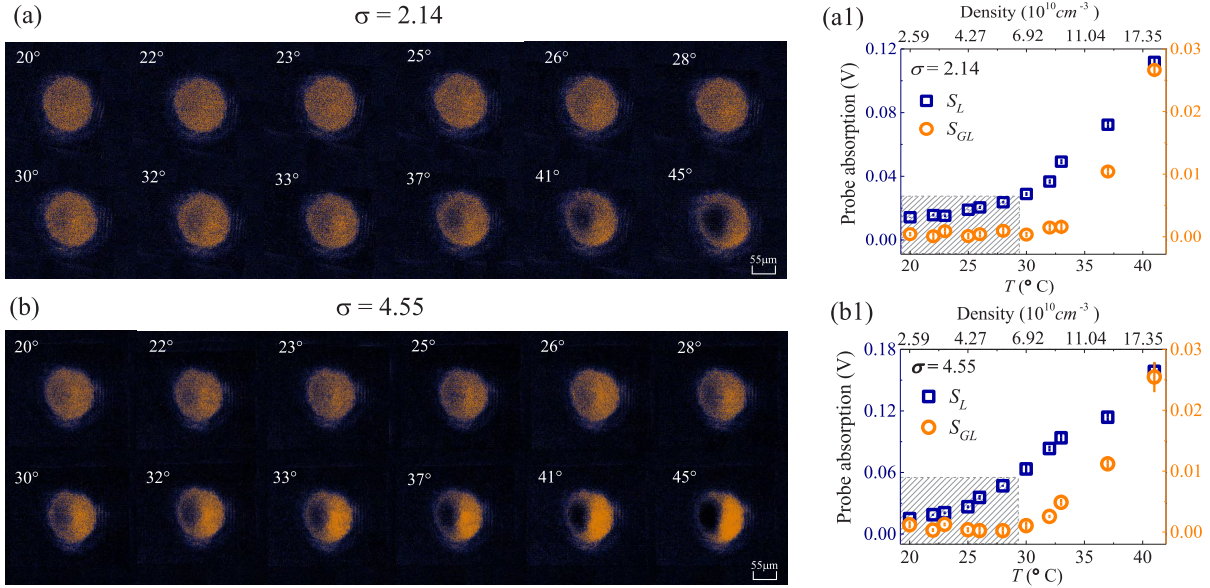


FIG. 2. Measurements of the partial \mathcal{PT} symmetry and its phase transition obtained by changing the atomic-cell temperature and the beam-waist ratio $\sigma \equiv w_c/w_p$. (a) The measured result of the probe intensity distribution for $\sigma = 2.14$: the probe beam displays uniform (nonuniform) intensity distribution for the temperature $T < 29^\circ\text{C}$ ($\gtrsim 29^\circ\text{C}$) as the system works with the partial \mathcal{PT} symmetry (nonpartial \mathcal{PT} symmetry). No partial \mathcal{PT} phase transition occurs in this case. (a1) Measured result of the probe absorption as a function of T (atomic density \mathcal{N}_a) with (orange circles) and without (blue squares) the repumping beam. S_{GL} (S_L): the PD signal in the presence (absence) of the repumping beam. Shaded region: the domain where the system works with the partial \mathcal{PT} symmetry. (b) and (b1) show similar measurements to (a) and (a1) but for $\sigma = 4.55$; the probe beam displays nonuniform intensity distribution for all temperatures as the system works in the broken phase of partial \mathcal{PT} symmetry (see the text for details).

symmetry. The physical reason behind this can be understood by shortening the atomic ground-state coherence lifetime, which is limited by the mean time of flight $\langle v \rangle_T/w_p$ of the atoms through the probe beam, where $\langle v \rangle_T = \sqrt{8k_B T/\pi m}$ (k_B is the Boltzmann constant and m is the atomic mass) is the mean atomic velocity at thermal equilibrium. When the atomic ground-state coherence lifetime decreases with the growth of temperature, an effective decay rate of the atomic ground state becomes more and more significant, leading eventually to the violation of partial \mathcal{PT} symmetry.

For comparison, the probe absorption in the absence of the repumping beam (i.e., signal S_L from PD) is also given by the blue squares in Fig. 2(a1), which increases with T (\mathcal{N}_a), indicating that the probe beam always suffers a significant loss and hence no partial \mathcal{PT} symmetry occurs. To observe the partial \mathcal{PT} symmetry and its phase transition in the system, we take σ as a tunable parameter and make new measurements. Plotted in Figs. 2(b) and 2(b1) are measured results similar to Figs. 2(a) and 2(a1) but for $\sigma = 4.55$. We see that in this situation the probe beam displays asymmetric intensity distributions for all temperatures [Fig. 2(b)]. Meanwhile, $S_{GL} \approx 0$ for $T < 29^\circ\text{C}$, meaning that the gain-loss balance is kept and the system works in a partially \mathcal{PT} -symmetric phase [the first row in Fig. 2(b) and the shaded region in Fig. 2(b1)]. Consequently, the nonuniformity of the probe intensity distribution for $T < 29^\circ\text{C}$ [the first row of Fig. 2(b)] must be the outcome by partial \mathcal{PT} symmetry breaking; i.e., the system has entered into a broken partially \mathcal{PT} -symmetric phase from the (unbroken) partially \mathcal{PT} -symmetric phase.

The above experimental findings can be analyzed quantitatively by defining the asymmetry degree of the probe intensity distribution,

$$D_{\text{asym}} = (I_{p, \text{right}} - I_{p, \text{left}})/(I_{p, \text{right}} + I_{p, \text{left}}), \quad (1)$$

where $I_{p, \text{left}}$ ($I_{p, \text{right}}$) is the average of the probe intensity in the left-half (right-half) part of the distribution, with $D_{\text{asym}} = 0$ and $D_{\text{asym}} \in (0, 1]$ characterizing uniform and nonuniform intensity distributions, respectively.

Measured (samples) and fitted (lines) results of D_{asym} as a function of T for $\sigma = 1.70, 2.14, 3.63, 3.95$, and 4.55 are shown in Fig. 3(a). We see that D_{asym} increases slowly with T ; however, it increases abruptly from zero when σ exceeds a critical value σ_{cr} . Illustrated in Fig. 3(b) are measured (samples) and calculated (lines) results of D_{asym} as a function of σ for $T = 24^\circ\text{C}, 26^\circ\text{C}$, and 28°C . It reveals clearly that a phase transition of partial \mathcal{PT} symmetry indeed occurs, with the EP locating at $\sigma = \sigma_{cr} \simeq 3.8$. Based on Figs. 3(a) and 3(b), a phase diagram is obtained by taking D_{asym} as a function of T and σ in Fig. 3(c), where domains of the unbroken, broken, and nonpartial \mathcal{PT} phases are displayed unambiguously.

III. THEORETICAL ANALYSIS AND EXAMPLES OF APPLICATIONS

A. Theoretical analysis and numerical simulations

To have a better understanding of the experimental results, we have also carried out theoretical analysis and numerical simulations based on Maxwell-Bloch (MB) equations, which describe both dynamics of atoms and probe beam propagation.

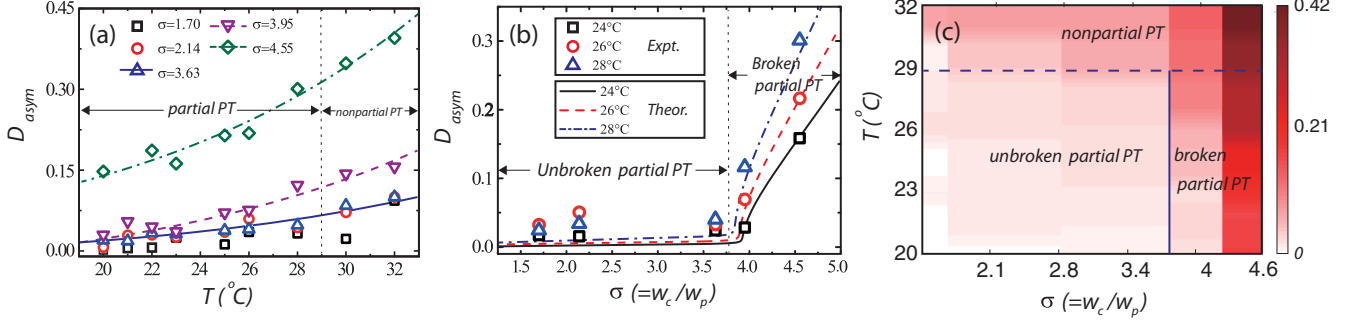


FIG. 3. Discrimination of the unbroken, broken, and nonpartial \mathcal{PT} phases. (a) Measurements (samples) and fittings (lines) of the asymmetry degree D_{asym} as a function of the temperature T for different beam-waist ratios (indicated in the figure). (b) Measurements (samples) and calculations (lines) of D_{asym} as a function of σ for different temperatures (indicated in the figure), where the EP locates at $\sigma = \sigma_{cr} \simeq 3.8$. (c) Phase diagram by taking D_{asym} as a function of T and σ , where domains of the unbroken, broken, and nonpartial \mathcal{PT} phases are shown. The solid (dashed) line indicates the boundary between domains of unbroken and broken (non)partial \mathcal{PT} phases.

Under electric-dipole and rotating-wave approximations, the Hamiltonian of the system with the repumping laser [as shown in Fig. 1(a)] in the interaction picture is given by

$$\hat{H}_{\text{int}} = -\hbar \sum_{j=2}^3 \Delta_j |j\rangle \langle j| - \hbar [(\Omega_p + \Omega_r e^{i\Delta_3 t}) |3\rangle \langle 1| + \Omega_c |3\rangle \langle 2| + \text{H.c.}], \quad (2)$$

where Ω_p , Ω_c , and Ω_r are half Rabi frequencies of the probe, control, and repumping lasers, defined respectively as $\Omega_p = (\mathbf{p}_{31} \cdot \mathbf{e}_p) \mathcal{E}_p / (2\hbar)$, $\Omega_c = (\mathbf{p}_{32} \cdot \mathbf{e}_c) \mathcal{E}_c / (2\hbar)$, and $\Omega_r = (\mathbf{p}_{41} \cdot \mathbf{e}_r) \mathcal{E}_r / (2\hbar)$, with \mathbf{p}_{ij} the electric dipole matrix element associated with the transition $|i\rangle \leftrightarrow |j\rangle$. The detunings are given by $\Delta_2 = \omega_p - \omega_c - (\omega_2 - \omega_1)$ and $\Delta_3 = \omega_p - (\omega_3 - \omega_1)$, with ω_j the eigenfrequency of the state $|j\rangle$.

The dynamics of the atoms is controlled by the optical Bloch equation

$$\frac{\partial \rho}{\partial t} = -\frac{i}{\hbar} [\hat{H}, \rho] - \Gamma [\rho], \quad (3)$$

where ρ is the density matrix, with the matrix elements $\rho_{\alpha\beta}$ ($\alpha, \beta = 1-3$) describing the atomic population ($\alpha = \beta$) and coherence ($\alpha \neq \beta$); Γ is the relaxation matrix, contributed from the spontaneous emission and dephasing. The equation of motion for the probe field Ω_p is obtained by the Maxwell equation. Under the slowly varying envelope approximation, it is reduced to the form

$$i \left(\frac{\partial}{\partial z} + \frac{1}{c} \frac{\partial}{\partial t} \right) \Omega_p + \frac{1}{2k_p} \nabla_{\perp}^2 \Omega_p + \kappa_{13} \rho_{31} = 0, \quad (4)$$

where $\nabla_{\perp}^2 = \partial_{xx} + \partial_{yy}$ and the coupling constant $\kappa_{13} = \mathcal{N}_a \omega_p p_{13}^2 / (2\epsilon_0 c \hbar)$, with \mathcal{N}_a the atomic concentration and c the light speed in vacuum. The second term on the left-hand side of the equation represents the diffraction of the probe beam. Both the control and the repumping fields are strong enough so that their half Rabi frequencies, Ω_c and Ω_r , can be considered as constants during the propagation of the probe field.

The Maxwell-Bloch equations (3) and (4) can be solved by using a perturbation method under the condition $\Omega_p \ll \Omega_c, \Omega_r$. The gain-loss property of the probe beam can be

obtained from the linear dispersion relation of the system (see Appendix B for more details).

For the convenience of following discussions, we rewrite the equation of motion for the probe field into a nondimensional form:

$$i \frac{\partial U}{\partial \zeta} = -d \left(\frac{\partial^2}{\partial \xi^2} + \frac{\partial^2}{\partial \eta^2} \right) U - V(\xi, \eta) U, \quad (5)$$

where the new variables are $(\xi, \eta) = (x, y) / w_p$ with w_p the $1/e^2$ waist of the probe laser beam, $\zeta = z/L$ with L the cell length ($L = 20$ mm in this work), $U(\xi, \eta, \zeta) = \Omega_p(x, y, z) / U_0$ with U_0 the typical Rabi frequency, $d = L / L_{\text{diff}}$ with $L_{\text{diff}} = 2w_p^2 k_p$ the characteristic diffraction length, and $V(\xi, \eta) = L \kappa_{13} \rho_{31} / \Omega_p$. The spatial dependence of the potential $V(\xi, \eta)$ is attributed to the spatial distribution of the control intensity.

According to the experiment, the intensity distribution of the control field is described by a Gaussian profile, $I_c(\xi, \eta) = I_{c0} e^{-(\xi^2 + \eta^2) / \sigma^2}$, with I_{c0} the maximum intensity and $\sigma \equiv w_c / w_p$ the beam-waist ratio of the control and probe beams. By using the approximation $I_c(\xi, \eta) \approx I_{c0} [1 - (\xi^2 + \eta^2) / \sigma^2]$, $V(\xi, \eta)$ can be written in the form $V(\xi, \eta) = V_1(\xi) + V_2(\eta)$, i.e., separable in the two transverse directions, where $V_1(\xi) = L(\beta_{G,L} \xi^2 + i\gamma_{G,L})$ and $V_2(\eta) = L\beta_{G,L} \eta^2$ (the subscript ‘‘G’’ for $\xi > 0$ and ‘‘L’’ for $\xi < 0$). Here, $\beta_{G,L} = \sigma^2 I_{c0} \text{Re}(\partial k_{G,L} / \partial I_c) |_{I_c=I_{c0}}$ and $\gamma_{G,L} = \text{Im}(k_{G,L} - \omega / c) |_{I_c=I_{c0}}$, with k_G (k_L) the linear dispersion relation with (without) the repumping laser (the explicit expressions of k_G and k_L are given in Appendix B). It should be pointed out that we have neglected the terms associated with $\text{Im}(\partial k_{G,L} / \partial I_c) |_{I_c=I_{c0}}$, which are rather small and can be regarded as high-order corrections.

Once the conditions

$$\beta_G = \beta_L = \beta, \quad \gamma_G = -\gamma_L = \gamma, \quad (6)$$

are fulfilled, the potential acquires the symmetry $V(\xi, \eta) = V^*(-\xi, \eta)$; i.e., $V(\xi, \eta)$ becomes a partially \mathcal{PT} -symmetric potential and can support all-real spectra (see Refs. [61–63]). The transition from the unbroken partial \mathcal{PT} phase to the broken one occurs when the ratio between the gain-loss coefficient and the phase shift, γ / β , is increased and across the EP. From the above expressions of β and γ , it is seen that γ / β is proportional to σ^2 but independent on the atomic density

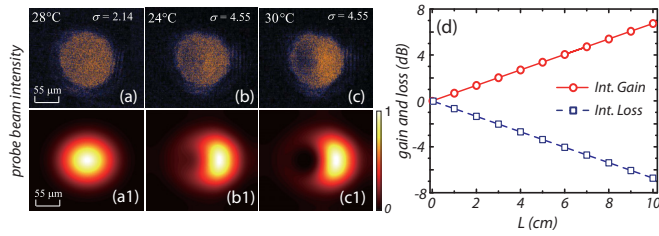


FIG. 4. The control of partial \mathcal{PT} symmetry and light amplification and attenuation. [(a)–(c)] Measured result [for different (σ, T)] of the probe intensity distribution, which is uniform in (a) due to the unbroken partial \mathcal{PT} symmetry, nonuniform in (b) due to the broken partial \mathcal{PT} symmetry, and nonuniform in (c) due to the nonpartial \mathcal{PT} symmetry. [(a1)–(c1)] Numerical results corresponding to (a)–(c). (d) Red circles (blue squares): The gain and loss of output probe intensity observed in the left (right) part of the probe beam as a function of the cell length L for $(\sigma, T) = (4.55, 28^\circ\text{C})$. The gain (loss) of the probe beam in the right (left) part arrives at 7 dB (–7 dB) at $L = 10$ cm.

\mathcal{N}_a (or the cell temperature T). Thus, by changing σ one can observe the phase transition of the partial \mathcal{PT} symmetry, which however will not happen by changing \mathcal{N}_a (or T).

For a further comparison between theory and experiment, in the left part of Fig. 4, we show the probe intensity distribution for $(\sigma, T) = (2.14, 28^\circ\text{C})$, $(4.55, 24^\circ\text{C})$, and $(4.55, 30^\circ\text{C})$, respectively. The first (second) row is the result given by experiment (theory). The distribution is uniform in Figs. 4(a) and 4(a1) due to the perfect \mathcal{PT} symmetry, nonuniform in Figs. 4(b) and 4(b1) due to the breaking of the partial \mathcal{PT} symmetry, and nonuniform in Figs. 4(c) and 4(c1) due to the nonpartial \mathcal{PT} symmetry. We see that the theory agrees with the experiment very well.

B. Examples of applications

The relation between the gain-loss coefficient γ and the asymmetry degree of the probe intensity, D_{asym} , is given by

$$\gamma = \ln[(1 + D_{\text{asym}})/(1 - D_{\text{asym}})]/(4L). \quad (7)$$

Since the measurement of D_{asym} can reach a high precision (relative standard deviation $\lesssim 5\%$), one can determine the location of EP rather precisely. Because the breaking of partial \mathcal{PT} symmetry depends only on σ but not T , the present system has a direct application in that it can be used to measure the probe beam waist precisely by tuning the control beam waist for $T < 29^\circ\text{C}$. The system is also promising for designing optical elements allowing light amplification in one half of a laser beam and attenuation in its other half. Figure 4(d) shows the output probe intensities respectively in the right (gain) and left (loss) parts as functions of L ; one sees that for a 10-cm-long cell with $(\sigma, T) = (4.55, 28^\circ\text{C})$, the increase (decrease) of the probe intensity in the right (left) part arrive at 7 dB (–7 dB).

IV. SUMMARY

In this work, we have carried out an experimental observation on partial \mathcal{PT} symmetry by using a laser-driven cesium atomic gas, where a two-dimensional partially

\mathcal{PT} -symmetric optical potential for a probe laser beam is created. The transition of the partial \mathcal{PT} symmetry from an unbroken phase to a broken one was observed through changing the beam-waist ratio of the control and probe laser beams; the unbroken, broken, and nonpartial \mathcal{PT} phases were discriminated unambiguously. Moreover, a technique for precisely determining the location of the EP was developed by measuring the asymmetry degree of the probe-beam intensity distribution. Besides, all experimental results have been verified well by theoretical analysis and numerical simulations. Our work paves the way for controlling multidimensional laser beams in non-Hermitian optical systems, and has potential applications for the precise measurement of the probe beam waist, as well as design of a combined light amplifier and attenuator in different parts of laser beams.

ACKNOWLEDGMENTS

J.Z. is supported by the National Key R&D Program of China (Grant No. 2017YFA0304203), the National Natural Science Foundation of China (Grants No. 61835007, No. 12120101004, and No. 62175136), Changjiang Scholars and Innovative Research Team University of Ministry of Education of China (Grant No. IRT_17R70) and 1331KSC. G.H., C.H., and Z.B. are supported by the National Natural Science Foundation of China (Grants No. 11975098, No. 11974117, and No. 11904104). C.H. is also supported by the National Key R&D Program of China (Grant No. 2017YFA0304201) and Municipal Science and Technology Major Project of Shanghai, China (Grant No. 2019SHDZX01).

APPENDIX A: EXPERIMENTAL MEASUREMENTS

1. The experimental setup and photodiode measurements

In the experiment, a weak probe (a strong control) laser couples the transition of $|6S_{1/2}, F = 3\rangle \rightarrow |6P_{3/2}, F' = 4\rangle$ ($|1\rangle \rightarrow |3\rangle$) [$|6S_{1/2}, F = 4\rangle \rightarrow |6P_{3/2}, F' = 4\rangle$ ($|2\rangle \rightarrow |3\rangle$)], forming a Λ -type three-level atom. Both lasers come from two external cavity lasers (ECLs; DLpro, Toptica) with their frequencies locked to related transitions and blue detuned by $\Delta_3/2\pi = 607$ MHz using double-passed acousto-optic modulators (AOMs) and meet the two-photon resonance condition $\Delta_2 = 0$. The control and probe lasers propagate through the atomic cell in the same direction. The strong repumping laser counterpropagates through the atomic cell and is locked to the transition $|6S_{1/2}, F = 3\rangle \rightarrow |6P_{3/2}, F' = 4\rangle$ ($|1\rangle \rightarrow |3\rangle$) in resonance.

The probe laser after passing through the vapor cell is detected by a photodiode (PD) for monitoring its gain and loss properties, as shown in Fig. 5. First, we measure the probe laser with frequency far detuned from the resonance corresponding to the signal p . In this case, the probe laser suffers no gain and no loss. Next, we measure the probe laser that propagates through the atoms driven by the control laser (without the repumping laser), corresponding to the signal $p + c$. In this case, although the system works under the condition of two-photon resonance, the probe laser suffers a small absorption (loss) due to the large detuning Δ_3 . Finally, we measure the probe laser that propagates through the atoms driven by both control and repumping lasers,

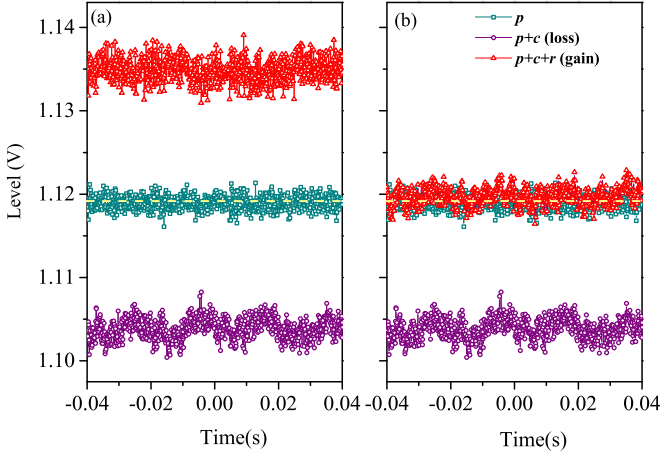


FIG. 5. The measurements of PD signals for monitoring the gain and loss properties of the probe laser. The signal p corresponds to the case that the probe laser propagates in the cell with the frequency far detuned from the resonance; $p+c$ corresponds to the case that the probe laser propagates in the atoms driven only by the control laser; $p+c+r$ corresponds to the case that the probe laser propagates in the atoms driven by both control and repumping lasers. Particularly, the repumping field is initially fully overlapped with the probe beam, in which the signals $p+c+r$ and $p+c$ are located symmetrically about the signal p , as shown in (a). The repumping field is then moved adiabatically to be half overlapped with the probe beam, in which the signal $p+c+r$ coincides with the signal p , as shown in (b).

corresponding to the signal $p+c+r$. Particularly, in this case, the repumping field is initially fully overlapped with the probe beam, resulting in a gain of the probe laser. By adjusting the system parameters carefully, it is possible to make the gain have the same magnitude with that of the loss without the repumping laser. Therefore, signals $p+c+r$ and $p+c$ are located symmetrically about the signal p , as shown in Fig. 5(a). After that, we move adiabatically the repumping field so that it is only half overlapped with the probe laser. Since the gain and loss are balanced now in different half regions of the probe beam, the signal $p+c+r$ coincides with

the signal p , as shown in Fig. 5(b), indicating that the probe laser suffers no gain and no loss as a whole. Thus, the partial \mathcal{PT} symmetry of the probe beam has been achieved.

2. The heating unit

In order to vary the atomic density, we put the atomic cell into a copper chamber that is heated to a certain temperature T via heating tapes. A multimeter (LINI-T-UT55) was used to measure the temperature of the cesium bubble, with an error $\pm 0.5^\circ$. The pressure of the atomic gases can be obtained from the equation [67]

$$\log_{10} P_V = 8.22127 - \frac{4006.048}{T} - 0.60194 \times 10^{-3} T - 0.19623 \log_{10} T, \quad (\text{A1})$$

where P_V is the pressure of the atomic vapor in Torr and T is the temperature in kelvins. The atomic density \mathcal{N}_a can be calculated by using the relation $\mathcal{N}_a = P_V / (k_B T)$, where k_B is the Boltzmann constant ($k_B = 1.38 \times 10^{-23}$ J/K).

Figures 6(a) and 6(b) show the heating unit in the experiment and the atomic density \mathcal{N}_a as a function of the temperature T , respectively. Some typical values of temperature T and corresponding atomic density \mathcal{N}_a used in the main text are given in Table I.

APPENDIX B: THEORETICAL ANALYSIS

1. Model and linear propagation of the probe field

The equations of motion for the density matrix elements (i.e., the optical Bloch equation) can be written as

$$i \frac{\partial}{\partial t} \rho_{11} - i\Gamma_{12} \rho_{22} - i\Gamma_{13} \rho_{33} + \Omega_{pr}^* \rho_{31} - \Omega_{pr} \rho_{31}^* = 0, \quad (\text{B1a})$$

$$i \frac{\partial}{\partial t} \rho_{22} + i\Gamma_{12} \rho_{22} - i\Gamma_{23} \rho_{33} + \Omega_c^* \rho_{32} - \Omega_c \rho_{32}^* = 0, \quad (\text{B1b})$$

$$i \frac{\partial}{\partial t} \rho_{33} + i\Gamma_3 \rho_{33} - \Omega_{pr}^* \rho_{31} + \Omega_{pr} \rho_{31}^* - \Omega_c^* \rho_{32} + \Omega_c \rho_{32}^* = 0, \quad (\text{B1c})$$

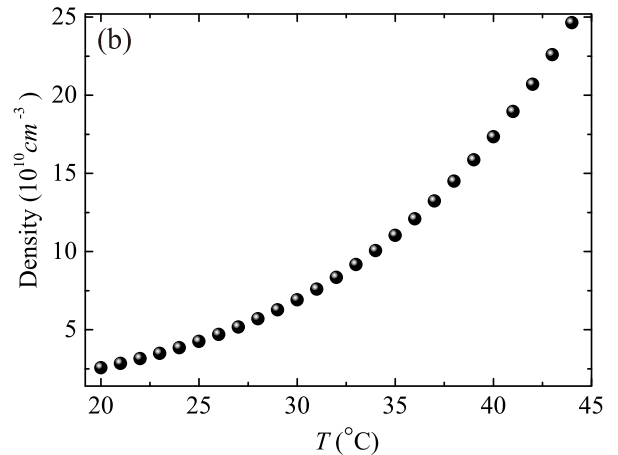
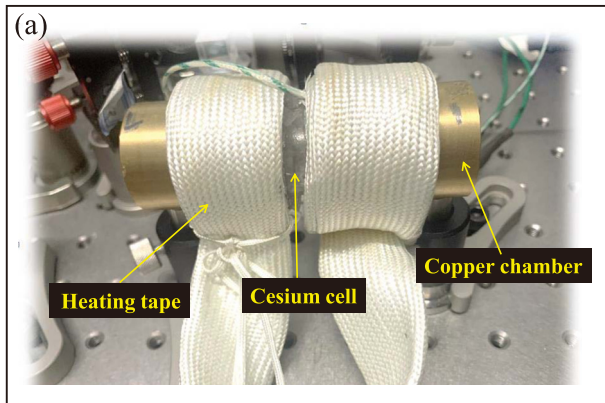


FIG. 6. The heating unit in the experiment. (a) The heating unit. The heating tape, the cesium cell, and the copper chamber in the unit are indicated, respectively. (b) The atomic density \mathcal{N}_a as a function of the temperature T .

TABLE I. Some typical values of temperature T and corresponding atomic density \mathcal{N}_a used in the main text.

Temperature, T ($^{\circ}\text{C}$)	20	22	24	26	28	29	30	32
Atomic density, \mathcal{N}_a ($\times 10^{10}$ cm^{-3})	2.59	3.17	3.87	4.71	5.72	6.29	6.92	8.36

for the diagonal elements, and

$$\left(i\frac{\partial}{\partial t} + d_{21}\right)\rho_{21} - \Omega_{pr}\rho_{32}^* + \Omega_c^*\rho_{31} = 0, \quad (\text{B2a})$$

$$\left(i\frac{\partial}{\partial t} + d_{31}\right)\rho_{31} - \Omega_{pr}(\rho_{33} - \rho_{11}) + \Omega_c\rho_{21} = 0, \quad (\text{B2b})$$

$$\left(i\frac{\partial}{\partial t} + d_{32}\right)\rho_{32} - \Omega_c(\rho_{33} - \rho_{22}) + \Omega_{pr}\rho_{21}^* = 0, \quad (\text{B2c})$$

for the nondiagonal elements, where $d_{lj} = \Delta_l - \Delta_j + i\gamma_{jl}$ ($j, l = 1, 2, 3$ and $\Delta_1 = 0$), with $\gamma_{jl} = (\Gamma_j + \Gamma_l)/2 + \gamma_{jl}^{\text{col}}$. Here, $\Gamma_j = \sum_{j' < l} \Gamma_{jl}$, with Γ_{jl} the spontaneous emission decay rate from $|l\rangle$ to $|j\rangle$ and γ_{jl}^{col} the dephasing rate reflecting the loss of phase coherence between $|j\rangle$ and $|l\rangle$ without

changing of population; the half Rabi frequency $\Omega_{pr} = \Omega_p + \Omega_r e^{i\Delta_3 t}$.

Since all lasers in the present system are continuous, the optical Bloch equations (B1) and (B2) can be solved in an adiabatic way (i.e., $\partial/\partial t \rightarrow 0$). Further, the probe beam is much weaker than the control and the repumping beams, i.e., $\Omega_p \ll \Omega_c, \Omega_r$, which allows us to use the perturbation theory by making the asymptotic expansions $\Omega_p = \sum_{n=0}^{\infty} \epsilon^n \Omega_p^{(n)}$ and $\rho_{ij} = \sum_{n=0}^{\infty} \epsilon^n \rho_{ij}^{(n)}$ ($i, j = 1, 2, 3$), where ϵ is a small parameter characterizing the small population depletion of the ground state. The leading-order solution (the base state) of the optical Bloch equations (B1) and (B2) is solved by setting $\Omega_p^{(0)} \approx 0$. By using the transformation $\rho_{21,31}^{(0)} = \varrho_{21,31}^{(0)} e^{i\Delta_3 t}$, we obtain the leading-order equations

$$\begin{pmatrix} -i\frac{\Gamma_{12}}{|\Omega_r|^2} - i2\text{Im}\left(\frac{\delta_{21}}{D}\right) & -i\frac{\Gamma_{13}}{|\Omega_r|^2} - i4\text{Im}\left(\frac{\delta_{21}}{D}\right) \\ i\Gamma_{12} & -i\Gamma_{23} \\ \Omega_c^*\left(\frac{1}{|\Omega_r|^2} + \frac{1}{D}\right) & -\Omega_c^*\left(\frac{1}{|\Omega_r|^2} - \frac{2}{D}\right) \\ \Omega_c\left(\frac{1}{|\Omega_r|^2} + \frac{1}{D^*}\right) & -\Omega_c\left(\frac{1}{|\Omega_r|^2} - \frac{2}{D^*}\right) \end{pmatrix} \begin{pmatrix} \frac{\Omega_c}{D} & -\frac{\Omega_c^*}{D^*} \\ -\Omega_c & \Omega_c^* \\ \frac{d_{32}^*}{|\Omega_r|^2} - \frac{\delta_{31}}{D} & 0 \\ 0 & \frac{d_{32}}{|\Omega_r|^2} - \frac{\delta_{31}^*}{D^*} \end{pmatrix} \begin{pmatrix} \rho_{22}^{(0)} \\ \rho_{33}^{(0)} \\ \rho_{23}^{(0)} \\ \rho_{32}^{(0)} \end{pmatrix} = \begin{pmatrix} -i2\text{Im}\left(\frac{\delta_{21}}{D}\right) \\ 0 \\ \frac{\Omega_c^*}{D} \\ \frac{\Omega_c}{D^*} \end{pmatrix}, \quad (\text{B3})$$

where $D = |\Omega_c|^2 - \delta_{21}\delta_{31}$, with $\delta_{21} = d_{21} - \Delta_3 = \Delta_2 - \Delta_3 + i\gamma_{12}$ and $\delta_{31} = d_{31} - \Delta_3 = i\gamma_{13}$. With the solutions of $\rho_{22}^{(0)}, \rho_{33}^{(0)}, \rho_{23}^{(0)}$, and $\rho_{32}^{(0)}$ at hand, other density matrix elements at the leading order can be obtained as

$$\rho_{11}^{(0)} = 1 - \rho_{22}^{(0)} - \rho_{33}^{(0)}, \quad (\text{B4a})$$

$$\rho_{21}^{(0)} = \Omega_r \frac{\Omega_c^*(\rho_{33}^{(0)} - \rho_{11}^{(0)}) - \delta_{31}\rho_{23}^{(0)}}{D} e^{i\Delta_3 t}, \quad (\text{B4b})$$

$$\rho_{31}^{(0)} = -\Omega_r \frac{\delta_{21}(\rho_{33}^{(0)} - \rho_{11}^{(0)}) - \Omega_c\rho_{23}^{(0)}}{D} e^{i\Delta_3 t}. \quad (\text{B4c})$$

It is obvious that at the limit $\Omega_r \rightarrow 0$, the leading-order solution will reduce to $\rho_{11}^{(0)} \approx 1$, with all other density matrix elements being zeros.

When the probe field is under consideration, the system undergoes a linear evolution. The first-order solution of the probe field can be sought by taking $\Omega_p^{(1)} = F(x, y)e^{ikz - i(\omega - \Delta_3)t}$, with $F(x, y)$ being a slowly varying envelope function of the probe field. By making the transformation $\rho_{21,31}^{(1)} = \varrho_{21,31}^{(1)} e^{ikz - i(\omega - \Delta_3)t}$, the optical Bloch equations (B1) and (B2) at the first order [at the order of $F(x, y)$] are given as

$$\begin{pmatrix} 0 & -\Gamma_{12} & -\Gamma_{13} \\ 0 & \Gamma_{12} & -\Gamma_{23} \\ 1 & 1 & 1 \end{pmatrix} \begin{pmatrix} \rho_{11}^{(1)} \\ \rho_{22}^{(1)} \\ \rho_{33}^{(1)} \end{pmatrix} = \begin{pmatrix} 2\text{Im}(F\varrho_{13}^{(0)} + \Omega_r\varrho_{13}^{(1)}) \\ 2\text{Im}(\Omega_c\rho_{23}^{(1)}) \\ 0 \end{pmatrix}, \quad (\text{B5})$$

and

$$\begin{pmatrix} \omega + \delta_{21} & \Omega_c^* & -\Omega_r \\ \Omega_c & \omega + \delta_{31} & 0 \\ \Omega_r^* & 0 & -\omega + d_{32}^* \end{pmatrix} \begin{pmatrix} \varrho_{21}^{(1)} \\ \varrho_{31}^{(1)} \\ \varrho_{23}^{(1)} \end{pmatrix} = \begin{pmatrix} F\rho_{23}^{(0)} \\ -F(\rho_{11}^{(0)} - \rho_{33}^{(0)}) - \Omega_r(\rho_{11}^{(1)} - \rho_{33}^{(1)}) \\ -F^*\varrho_{21}^{(0)} - \Omega_c^*(\rho_{22}^{(1)} - \rho_{33}^{(1)}) \end{pmatrix}. \quad (\text{B6})$$

Equations (B5) and (B6) should be solved simultaneously, giving the solution of $\varrho_{31}^{(1)}$ in terms of F and F^* (the expression is rather lengthy and omitted here). From the substitution of $\varrho_{31}^{(1)}$ into the Maxwell equation (4) without including the diffraction (which is a high-order effect), one can readily obtain the linear dispersion relation $k(\omega)$ of the system.

Particularly, if a set of parameters can be found so that $\rho_{jj}^{(1)} \approx \varrho_{21}^{(0)} \approx 0$ ($j = 1, 2, 3$), the solution of $\varrho_{31}^{(1)}$ can be significantly simplified, reading as

$$\rho_{31}^{(1)} = \frac{X(\rho_{33}^{(0)} - \rho_{11}^{(0)}) + \Omega_c(\omega - d_{32}^*)\rho_{23}^{(0)}}{Y} F e^{ikz - i(\omega - \Delta_3)t}, \quad (\text{B7})$$

where $X = |\Omega_r|^2 - (\omega + \delta_{21})(\omega - d_{32}^*)$ and $Y = |\Omega_r|^2(\omega + \delta_{31}) + |\Omega_c|^2(\omega - d_{32}^*) - (\omega + \delta_{21})(\omega + \delta_{31})(\omega - d_{32}^*)$. With the solution (B7), one can obtain the linear dispersion relation $k(\omega)$:

$$k(\omega) = \frac{\omega - \Delta_3}{c} + \kappa_{13} \frac{X(\rho_{33}^{(0)} - \rho_{11}^{(0)}) + \Omega_c(\omega - d_{32}^*)\rho_{23}^{(0)}}{Y}. \quad (\text{B8})$$

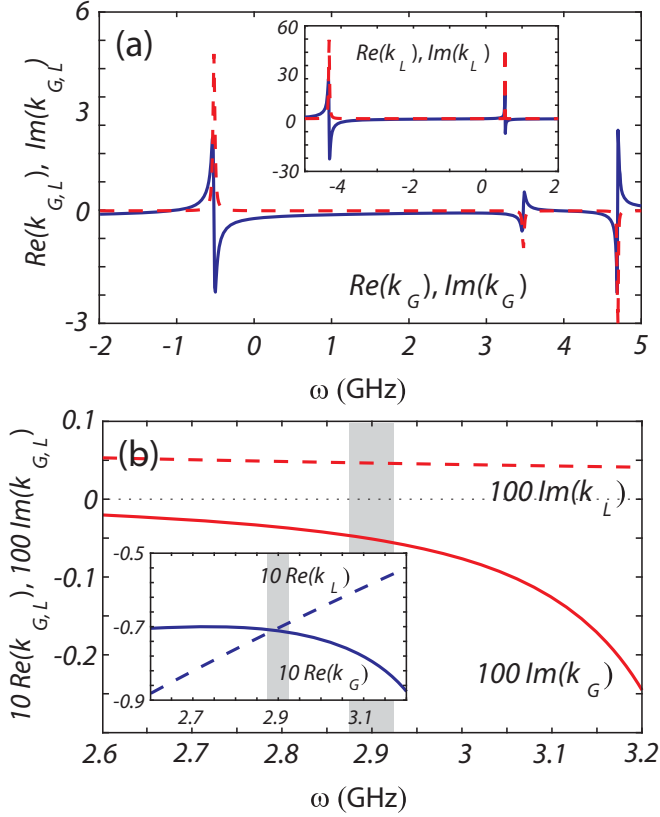


FIG. 7. (a) The real and imaginary parts of the linear dispersion relation with the repumping field (the gain-channel dispersion relation), $Re(k_G)$ (blue solid line) and $Im(k_G)$ (red dashed line), as functions of ω . Inset: The real and imaginary parts of the linear dispersion relation without the repumping field (the loss-channel dispersion relation), $Re(k_L)$ (blue solid line) and $Im(k_L)$ (red dashed line), as functions of ω . (b) The details of the linear dispersion relation around $\omega = 2.8$ GHz. $Im(k_G)$ (red solid line) and $Im(k_L)$ (red dashed line) are plotted as functions of ω , enlarged by 100 times. $-Im(k_G) \approx Im(k_L)$ at $\omega \approx 2.87$ GHz. Inset: $Re(k_G)$ (red solid line) and $Re(k_L)$ (red dashed line) are plotted as functions of ω , enlarged by 10 times. $Re(k_G) \approx Re(k_L)$ at $\omega \approx 2.87$ GHz.

Since the imaginary part of the linear dispersion $k(\omega)$ in the presence of the repumping field can be negative in some ω intervals, corresponding to an optical gain acquired by the probe field, $k(\omega)$ is referred to as the gain-channel dispersion relation, denoted by $k_G(\omega)$ (“G” means the gain).

The above model can be realized by using the ^{133}Cs atoms as described in the main text, in which the decay rates are $\Gamma_2 \approx 2\pi \times 1$ kHz and $\Gamma_3 \approx 2\pi \times 5.2$ MHz; the electric dipole matrix elements are $p_{13} \approx 3.8 \times 10^{-27}$ C cm [67]. Moreover, we take the atomic density $N_a \approx 2.59 \times 10^{10}$ cm $^{-3}$ ($T = 20^\circ\text{C}$), the Rabi frequencies $\Omega_c = 2\pi \times 239.14$ MHz and $\Omega_r = 2\pi \times 93.33$ MHz, and the detunings $\Delta_2 = 0$ MHz and $\Delta_3 = 2\pi \times 607$ MHz.

Figure 7(a) shows the real and imaginary parts of the gain-channel dispersion relation k_G , $Re(k_G)$ and $Im(k_G)$, as functions of ω , which represent the phase shift and gain [$Im(k_G) < 0$] or loss [$Im(k_G) > 0$], respectively. From this figure, we note that $Im(k_G)$ becomes negative and hence the probe field acquires an optical gain for $\omega \gtrsim 2$ GHz.

Additionally, $Re(k_G)$ is negative, meaning that the probe field acquires a negative phase shift, in a large frequency interval $0.5 \lesssim \omega \lesssim 3.5$ GHz.

In the absence of the repumping field, the system is reduced to a standard Λ -type configuration. In this case, the Hamiltonian and the optical Bloch equations can be readily obtained from Eqs. (2), (B1), and (B2) by setting $\Omega_r = 0$. Now the leading-order solution is given by $\rho_{11}^{(0)} = 1$, with all other density matrix elements being zeros while the linear dispersion relation $k(\omega)$ is obtained as

$$k(\omega) = \frac{\omega}{c} + \kappa_{13} \frac{\omega + d_{21}}{|\Omega_c|^2 - (\omega + d_{21})(\omega + d_{31})}. \quad (\text{B9})$$

Since the imaginary part of $k(\omega)$ without the repumping field is always positive, corresponding to an optical absorption (loss) of the probe field, $k(\omega)$ is referred to as the loss-channel dispersion relation, denoted by $k_L(\omega)$ (“L” means the loss).

The real and imaginary parts of the loss-channel dispersion relation k_L , $Re(k_L)$ and $Im(k_L)$, as functions of ω , are illustrated in the inset of Fig. 7(a). The parameters are the same with those used in the case of the gain configuration (in the presence of Ω_r). We see that although the transparency window is widely opened due to the electromagnetically induced transparency effect, the probe field still suffers a small loss as $Im[k_L(\omega = 0)] > 0$ in the whole range of ω .

In Fig. 7(b), we show the details of the linear dispersion relation around $\omega = 2.8$ GHz. Both $Im(k_G)$ and $Im(k_L)$ are illustrated as functions of ω . In order to observe more clearly, they are enlarged by 100 times. It is seen that $-Im(k_G) \approx Im(k_L) \approx 0.5 \times 10^{-3}$ cm $^{-1}$ at $\omega \approx 2.87$ GHz. The inset of the figure shows $Re(k_G)$ and $Re(k_L)$ as functions of ω , enlarged by 10 times. It is seen that $Re(k_G) \approx Re(k_L) \approx -0.07$ cm $^{-1}$ at the same value of ω . Thus, we find that with the parameters given above, when $\omega \approx 2.8$ GHz, one has $-Im(k_G) \approx Im(k_L) \approx 0.5 \times 10^{-3}$ cm $^{-1}$ and $Re(k_G) \approx Re(k_L) \approx -0.07$ cm $^{-1}$, simultaneously. This is crucial for the realization of partial \mathcal{PT} symmetry in the present system, as shown below.

The partial \mathcal{PT} symmetry can be realized by using the linear dispersion relations of the gain and loss channels described above. Particularly, when the system works in the gain channel, the last term on the left-hand side of Eq. (4) reads $\kappa_{13}\rho_{31} = [k_G - (\omega - \Delta_3)/c]\Omega_p$ and the probe field can acquire a gain. On the contrary, when the system works in the loss channel, the last term on the left-hand side of Eq. (4) reads $\kappa_{13}\rho_{31} = (k_L - \omega/c)\Omega_p$ and the probe field acquires only a loss. By tuning the parameters carefully, it is possible to make the gain and loss balance each other.

2. Estimation of the Doppler effect

For a warm atomic vapor, the inhomogeneous broadening of the atomic radiation spectrum line due to the Doppler effect can play an important role in the optical response of the system. To include this effect, the external motion of the atoms must be taken into account and Hamiltonian (2) should

be replaced with

$$\hat{H}_{\text{int}} = -\hbar \sum_{j=2}^3 \Delta_j |j\rangle \langle j| - \hbar [(\Omega_p e^{ik_p vt} + \Omega_r e^{i(k_r v + \Delta_3)t}) \times |3\rangle \langle 1| + \Omega_c e^{ik_c vt} |3\rangle \langle 2| + \text{H.c.}], \quad (\text{B10})$$

where v is the z component of the atomic velocity \mathbf{v} . According to Hamiltonian (B10), the optical Bloch equations are given by Eqs. (B1) and (B2) but $d_{21} = -(k_p - k_c)v + \Delta_2 + i\gamma_{12}$, $d_{31} = -k_p v + \Delta_3 + i\gamma_{13}$, and $d_{32} = -k_c v + \Delta_3 - \Delta_2 + i\gamma_{23}$.

Since $k_p \approx k_c$ due to the copropagating probe and the control beams, the term $-(k_p - k_c)v$ in the expression of d_{21} is approximately zero and hence d_{21} is not affected by the Doppler effect. Moreover, under the conditions of two-photon

resonance ($\Delta_2 \approx 0$) and a very large single-photon detuning ($\Delta_3 \gg k_p v \approx k_c v$), the terms $-k_p v$ and $-k_c v$ in the expressions of d_{31} and d_{32} can also be neglected and hence d_{31} and d_{32} are not affected much by the Doppler effect.

It is convenient to define the Doppler width $\Delta\omega_D = k_p v_T$, where $v_T = (2k_B T/M)^{1/2}$ is the most probable atomic speed at temperature T , with k_B the Boltzmann constant and M the atomic mass. Then, the condition of a very large single-photon detuning can be written as $\Delta_3 \gg \Delta\omega_D$. In the system under study, the probe and the control beams are copropagating and the detunings are taken as $\Delta_2 \approx 0$ and $\Delta_3 = 2\pi \times 607$ MHz which is much larger than the typical value of the Doppler width for a cesium atom at room temperature, $\Delta\omega_D \approx 400$ MHz [68]. Due to the above reasons, the Doppler integral is not included in the theoretical treatment for simplicity.

-
- [1] C. M. Bender and S. Boettcher, Real Spectra in Non-Hermitian Hamiltonians Having PT Symmetry, *Phys. Rev. Lett.* **80**, 5243 (1998).
- [2] C. M. Bender, Introduction to PT-symmetric quantum theory, *Contemp. Phys.* **46**, 277 (2005).
- [3] C. M. Bender, Making sense of non-Hermitian Hamiltonians, *Rep. Prog. Phys.* **70**, 947 (2007).
- [4] V. V. Konotop, J. Yang, and D. A. Zezyulin, Nonlinear waves in PT-symmetric systems, *Rev. Mod. Phys.* **88**, 035002 (2016).
- [5] R. El-Ganainy, K. G. Makris, M. Khajavikhan, Z. H. Musslimani, S. Rotter, and D. N. Christodoulides, Non-Hermitian physics and PT symmetry, *Nat. Phys.* **14**, 11 (2018).
- [6] Y. Ashida, Z. Gong, and M. Ueda, Non-Hermitian physics, *Adv. Phys.* **69**, 249 (2020).
- [7] S. Klaiman and L. S. Cederbaum, Non-Hermitian Hamiltonians with space-time symmetry, *Phys. Rev. A* **78**, 062113 (2008).
- [8] R. El-Ganainy, K. G. Makris, D. N. Christodoulides, and Z. H. Musslimani, Theory of coupled optical PT-symmetric structures, *Opt. Lett.* **32**, 2632 (2007).
- [9] Z. H. Musslimani, K. G. Makris, R. El-Ganainy, and D. N. Christodoulides, Optical Solitons in PT Periodic Potentials, *Phys. Rev. Lett.* **100**, 030402 (2008).
- [10] K. G. Makris, R. El-Ganainy, D. N. Christodoulides, and Z. H. Musslimani, Beam Dynamics in PT Symmetric Optical Lattices, *Phys. Rev. Lett.* **100**, 103904 (2008).
- [11] L. Feng, R. El-Ganainy, and L. Ge, Non-Hermitian photonics based on parity-time symmetry, *Nat. Photonics* **11**, 752 (2017).
- [12] A. Guo, G. J. Salamo, D. Duchesne, R. Morandotti, M. Volatier-Ravat, V. Aimez, G. A. Siviloglou, and D. N. Christodoulides, Observation of PT-Symmetry Breaking in Complex Optical Potentials, *Phys. Rev. Lett.* **103**, 093902 (2009).
- [13] C. E. Rüter, K. G. Makris, R. El-Ganainy, D. N. Christodoulides, M. Segev, and D. Kip, Observation of parity-time symmetry in optics, *Nat. Phys.* **6**, 192 (2010).
- [14] A. Szameit, M. C. Rechtsman, O. Bahat-Treidel, and M. Segev, PT-symmetry in honeycomb photonic lattices, *Phys. Rev. A* **84**, 021806(R) (2011).
- [15] L. Feng, M. Ayache, J. Huang, Y.-L. Xu, M.-H. Lu, Y.-F. Chen, Y. Fainman, and A. Scherer, Nonreciprocal light propagation in a silicon photonic circuit, *Science* **333**, 729 (2011).
- [16] A. Regensburger, C. Bersch, M. Miri, G. Onishchukov, D. N. Christodoulides, and U. Peschel, Parity-time synthetic photonic lattices, *Nature (London)* **488**, 167 (2012).
- [17] B. Peng, Ş. K. Özdemir, F. Lei, F. Monifi, M. Gianfreda, G. L. Long, S. Fan, F. Nori, C. M. Bender, and L. Yang, Parity-time-symmetric whispering-gallery microcavities, *Nat. Phys.* **10**, 394 (2014).
- [18] L. Chang, X. Jiang, S. Hua, C. Yang, J. Wen, L. Jiang, G. Li, G. Wang, and M. Xiao, Parity-time symmetry and variable optical isolation in active-passive-coupled microresonators, *Nat. Photonics* **8**, 524 (2014).
- [19] J. Wen, X. Jiang, L. Jiang, and M. Xiao, Parity-time symmetry in optical microcavity systems, *J. Phys. B: At. Mol. Opt. Phys.* **51**, 222001 (2018).
- [20] L. Ding, K. Shi, Q. Zhang, D. Shen, X. Zhang, and W. Zhang, Experimental Determination of \mathcal{PT} -Symmetric Exceptional Points in a Single Trapped Ion, *Phys. Rev. Lett.* **126**, 083604 (2021).
- [21] C. Hang, G. Huang, and V. V. Konotop, \mathcal{PT} Symmetry with a System of Three-Level Atoms, *Phys. Rev. Lett.* **110**, 083604 (2013).
- [22] J. Sheng, M.-A. Miri, D. N. Christodoulides, and M. Xiao, \mathcal{PT} -symmetric optical potentials in a coherent atomic medium, *Phys. Rev. A* **88**, 041803(R) (2013).
- [23] P. Peng, W. Cao, C. Shen, W. Qu, J. Wen, L. Jiang, and Y. Xiao, Anti-parity-time symmetry with flying atoms, *Nat. Phys.* **12**, 1139 (2016).
- [24] Z. Zhang, Y. Zhang, J. Sheng, L. Yang, M.-A. Miri, D. N. Christodoulides, B. He, Y. Zhang, and M. Xiao, Observation of Parity-Time Symmetry in Optically Induced Atomic Lattices, *Phys. Rev. Lett.* **117**, 123601 (2016).
- [25] R. Wen, C.-L. Zou, X. Zhu, P. Chen, Z. Y. Ou, J. F. Chen, and W. Zhang, Non-Hermitian Magnon-Photon Interference in an Atomic Ensemble, *Phys. Rev. Lett.* **122**, 253602 (2019).
- [26] Y. Jiang, Y. Mei, Y. Zuo, Y. Zhai, J. Li, J. Wen, and S. Du, Anti-Parity-Time Symmetric Optical Four-Wave Mixing in Cold Atoms, *Phys. Rev. Lett.* **123**, 193604 (2019).
- [27] C. Hang and G. Huang, Parity-time symmetry with coherent atomic gases, *Adv. Phys.-X* **2**, 737 (2017).
- [28] Z. Zhang, D. Ma, J. Sheng, Y. Zhang, Y. Zhang, and M. Xiao, Non-Hermitian optics in atomic systems, *J. Phys. B: At. Mol. Opt. Phys.* **51**, 072001 (2018).

- [29] W. Heiss, The physics of exceptional points, *J. Phys. A: Math. Theor.* **45**, 444016 (2012).
- [30] M.-A. Miri and A. Alù, Exceptional points in optics and photonics, *Science* **363**, eaar7709 (2019).
- [31] S. Longhi, Bloch Oscillations in Complex Crystals with \mathcal{PT} Symmetry, *Phys. Rev. Lett.* **103**, 123601 (2009).
- [32] M. Wimmer, M. A. Miri, D. Christodoulides, and U. Peschel, Observation of Bloch oscillations in complex PT-symmetric photonic lattices, *Sci. Rep.* **5**, 17760 (2015).
- [33] H. Ramezani, T. Kottos, R. El-Ganainy, and D. N. Christodoulides, Unidirectional nonlinear \mathcal{PT} -symmetric optical structures, *Phys. Rev. A* **82**, 043803 (2010).
- [34] Z. Lin, H. Ramezani, T. Eichelkraut, T. Kottos, H. Cao, and D. N. Christodoulides, Unidirectional Invisibility Induced by \mathcal{PT} -Symmetric Periodic Structures, *Phys. Rev. Lett.* **106**, 213901 (2011).
- [35] S. Longhi, \mathcal{PT} -symmetric laser absorber, *Phys. Rev. A* **82**, 031801(R) (2010).
- [36] Y. D. Chong, L. Ge, and A. D. Stone, \mathcal{PT} -Symmetry Breaking and Laser-Absorber Modes in Optical Scattering Systems, *Phys. Rev. Lett.* **106**, 093902 (2011).
- [37] Y. Sun, W. Tan, H. Li, J. Li, and H. Chen, Experimental Demonstration of a Coherent Perfect Absorber with PT Phase Transition, *Phys. Rev. Lett.* **112**, 143903 (2014).
- [38] C. Hang, G. Huang, and V. V. Konotop, Tunable spectral singularities: Coherent perfect absorber and laser in an atomic medium, *New J. Phys.* **18**, 085003 (2016).
- [39] V. V. Konotop, V. S. Shchesnovich, and D. A. Zezyulin, Giant amplification of modes in parity-time symmetric waveguides, *Phys. Lett. A* **376**, 2750 (2012).
- [40] L. Feng, Z. J. Wong, R. Ma, Y. Wang, and X. Zhang, Single-mode laser by parity-time symmetry breaking, *Science* **346**, 972 (2014).
- [41] H. Hodaie, M.-A. Miri, M. Heinrich, D. N. Christodoulides, and M. Khajavikhan, Parity-time-symmetric microring lasers, *Science* **346**, 975 (2014).
- [42] H. Jing, S. K. Özdemir, X.-Y. Lü, J. Zhang, L. Yang, and F. Nori, \mathcal{PT} -Symmetric Phonon Laser, *Phys. Rev. Lett.* **113**, 053604 (2014).
- [43] J. Zhang, B. Peng, Ş. K. Özdemir, K. Pichler, D. O. Krimer, G. Zhao, F. Nori, Y.-X. Liu, S. Rotter, and L. Yang, A phonon laser operating at an exceptional point, *Nat. Photonics* **12**, 479 (2018).
- [44] H. Xu, D. Mason, L. Jiang, and J. G. E. Harris, Topological energy transfer in an optomechanical system with exceptional points, *Nature (London)* **537**, 80 (2016).
- [45] J. Doppler, A. A. Mailybaev, J. Böhm, U. Kuhl, A. Girschik, F. Libisch, T. J. Milburn, P. Rabl, N. Moiseyev, and S. Rotter, Dynamically encircling an exceptional point for asymmetric mode switching, *Nature (London)* **537**, 76 (2016).
- [46] W. Chen, Ş. K. Özdemir, G. Zhao, J. Wiersig, and L. Yang, Exceptional points enhance sensing in an optical microcavity, *Nature (London)* **548**, 192 (2017).
- [47] Y.-M. Liu, F. Gao, C.-H. Fan, and J.-H. Wu, Asymmetric light diffraction of an atomic grating with PT symmetry, *Opt. Lett.* **42**, 4283 (2017).
- [48] T. Shui, W.-X. Yang, S. Liu, L. Li, and Z. Zhu, Asymmetric diffraction by atomic gratings with optical \mathcal{PT} symmetry in the Raman-Nath regime, *Phys. Rev. A* **97**, 033819 (2018).
- [49] L. Xiao, X. Zhan, Z. H. Bian, K. K. Wang, X. Zhang, X. P. Wang, J. Li, K. Mochizuki, D. Kim, N. Kawakami, W. Yi, H. Obuse, B. C. Sanders, and P. Xue, Observation of topological edge states in parity-time-symmetric quantum walks, *Nat. Phys.* **13**, 1117 (2017).
- [50] M. Naghiloo, M. Abbasi, Y. N. Joglekar, and K. W. Murch, Quantum state tomography across the exceptional point in a single dissipative qubit, *Nat. Phys.* **15**, 1232 (2019).
- [51] J. Li, A. K. Harter, J. Liu, L. de Melo, Y. N. Joglekar, and L. Luo, Observation of parity-time symmetry breaking transitions in a dissipative Floquet system of ultracold atoms, *Nat. Commun.* **10**, 855 (2019).
- [52] Y. Li, Y. Peng, L. Han, M. Miri, W. Li, M. Xiao, X. Zhu, J. Zhao, A. Alù, S. Fan, and C. Qiu, Anti-parity-time symmetry in diffusive systems, *Science* **364**, 170 (2019).
- [53] A. Zenesini, H. Lignier, D. Ciampini, O. Morsch, and E. Arimondo, Coherent Control of Dressed Matter Waves, *Phys. Rev. Lett.* **102**, 100403 (2009).
- [54] R. Frank, Population trapping and inversion in ultracold Fermi gases by excitation of the optical lattice: Non-equilibrium Floquet-Keldysh description, *Appl. Phys. B* **113**, 41 (2013).
- [55] R. Frank, Quantum criticality and population trapping of fermions by non-equilibrium lattice modulation, *New J. Phys.* **15**, 123030 (2013).
- [56] A. Eckardt, Atomic quantum gases in periodically driven optical lattices, *Rev. Mod. Phys.* **89**, 011004 (2017).
- [57] C. Gross and I. Bloch, Quantum simulations with ultracold atoms in optical lattices, *Science* **357**, 995 (2017).
- [58] D. Mayer, F. Schmidt, S. Haupt, Q. Bouton, D. Adam, T. Lausch, E. Lutz, and A. Widera, Nonequilibrium thermodynamics and optimal cooling of a dilute atomic gas, *Phys. Rev. Research* **2**, 023245 (2020).
- [59] L. Xiao, T. Deng, K. Wang, G. Zhu, Z. Wang, W. Yi, and P. Xue, Non-Hermitian bulk-boundary correspondence in quantum dynamics, *Nat. Phys.* **16**, 761 (2020).
- [60] L. Xiao, T. Deng, K. Wang, Z. Wang, W. Yi, and P. Xue, Observation of Non-Bloch Parity-Time Symmetry and Exceptional Points, *Phys. Rev. Lett.* **126**, 230402 (2021).
- [61] J. Yang, Partially PT symmetric optical potentials with all-real spectra and soliton families in multidimensions, *Opt. Lett.* **39**, 1133 (2014).
- [62] Y. V. Kartashov, V. V. Konotop, and L. Torner, Topological States in Partially- \mathcal{PT} -Symmetric Azimuthal Potentials, *Phys. Rev. Lett.* **115**, 193902 (2015).
- [63] H. Wang, J. Huang, X. Ren, Y. Weng, D. Mihalache, and Y. He, Families of dipole solitons in self-defocusing Kerr media and partial parity-time-symmetric optical potentials, *Rom. J. Phys.* **63**, 205 (2018).
- [64] L. Ge and A. D. Stone, Parity-Time Symmetry Breaking beyond One Dimension: The Role of Degeneracy, *Phys. Rev. X* **4**, 031011 (2014).
- [65] To realize the optical potential with partial \mathcal{PT} symmetry, we should consider the control intensity distribution; i.e., Ω_c is taken to be (x, y) dependent (see Appendix B for more details).
- [66] This value of temperature, $T = 29^\circ\text{C}$, is not a critical temperature because no symmetry breaking (phase transition) occurs in this process. In fact, the signal S_{GL} increases smoothly with the growth of T even in the range $0^\circ\text{C} < T < 29^\circ\text{C}$ and the increment of S_{GL} becomes *appreciable* when $T \gtrsim 29^\circ\text{C}$. Moreover,

this value of temperature depends on the length of the atomic cell.

- [67] D. A. Steck, Cesium D Line Data, <http://steck.us/alkalidata> (revision 1.6, 14 October 2003).
- [68] V. Vuletić, V. A. Sautenkov, C. Zimmermann, and T. W. Hänsch, Measurement of cesium resonance line self-broadening and shift with Doppler-free selective reflection spectroscopy, *Opt. Commun.* **99**, 185 (1993).